

## Quasi continuous wave laser sintering of Si-Ge nanoparticles for thermoelectrics

Kai Xie, Kelsey Mork, Jacob T. Held, K. Andre Mkhoyan, Uwe Kortshagen, and Mool C. Gupta

Citation: *Journal of Applied Physics* **123**, 094301 (2018); doi: 10.1063/1.5018337

View online: <https://doi.org/10.1063/1.5018337>

View Table of Contents: <http://aip.scitation.org/toc/jap/123/9>

Published by the [American Institute of Physics](#)

---

### Articles you may be interested in

[Ultrahigh thermal conductivity of isotopically enriched silicon](#)

*Journal of Applied Physics* **123**, 095112 (2018); 10.1063/1.5017778

[Perspective: Acoustic metamaterials in transition](#)

*Journal of Applied Physics* **123**, 090901 (2018); 10.1063/1.5007682

[Dual-wavelength GaSb-based mid infrared photonic crystal surface emitting lasers](#)

*Journal of Applied Physics* **123**, 093102 (2018); 10.1063/1.5012113

[Effect of thermal annealing on the redistribution of alkali metals in Cu\(In,Ga\)Se<sub>2</sub> solar cells on glass substrate](#)

*Journal of Applied Physics* **123**, 093101 (2018); 10.1063/1.5016949

[Broadband low-frequency sound isolation by lightweight adaptive metamaterials](#)

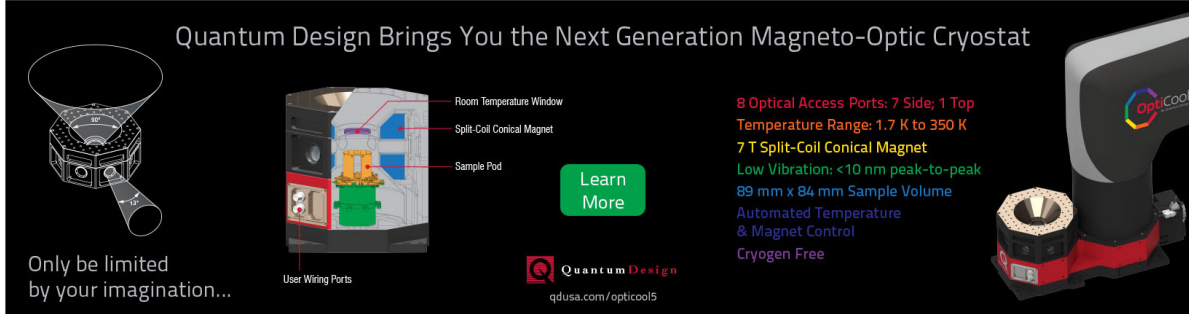
*Journal of Applied Physics* **123**, 091705 (2018); 10.1063/1.5011251

[Negative magnetization and the sign reversal of exchange bias field in Co\(Cr<sub>1-x</sub>Mn<sub>x</sub>\)<sub>2</sub>O<sub>4</sub> \(0 ≤ x ≤ 0.6\)](#)

*Journal of Applied Physics* **123**, 093902 (2018); 10.1063/1.5009404

---

Quantum Design Brings You the Next Generation Magneto-Optic Cryostat



Only be limited by your imagination...

Room Temperature Window  
Split-Coil Conical Magnet  
Sample Pod  
User Wiring Ports

[Learn More](#)

Quantum Design  
qdusa.com/opticool5

8 Optical Access Ports: 7 Side; 1 Top  
Temperature Range: 1.7 K to 350 K  
7 T Split-Coil Conical Magnet  
Low Vibration: <10 nm peak-to-peak  
89 mm x 84 mm Sample Volume  
Automated Temperature & Magnet Control  
Cryogen Free

# Quasi continuous wave laser sintering of Si-Ge nanoparticles for thermoelectrics

Kai Xie,<sup>1</sup> Kelsey Mork,<sup>2</sup> Jacob T. Held,<sup>3</sup> K. Andre Mkhoyan,<sup>3</sup> Uwe Kortshagen,<sup>2</sup> and Mool C. Gupta<sup>1,a)</sup>

<sup>1</sup>Department of Electrical and Computer Engineering, University of Virginia, Charlottesville 22904, USA

<sup>2</sup>Department of Mechanical Engineering, University of Minnesota, Minnesota 55455, USA

<sup>3</sup>Department of Chemical Engineering and Materials Science, University of Minnesota, Minnesota 55455, USA

(Received 5 December 2017; accepted 13 February 2018; published online 2 March 2018)

Silicon-germanium is an important thermoelectric material for high temperature applications. In this study, thin films composed of SiGe nanoparticles were synthesized in a plasma reactor and sintered by a millisecond pulse width, quasi continuous wave, near infrared laser of wavelength 1070 nm. We demonstrate that laser sintered SiGe thin films have high electrical and low thermal conductivity, dependent on the surface morphology and dopant concentration. Substrate wetting of laser heating induced molten SiGe was found to play an important role in the final surface morphology of the films. Interconnected percolation structures, formed when proper substrate wetting occurs, were found to be more conductive than the balling structure that formed with insufficient wetting. Laser power was adjusted to maximize dopant reactivation while still minimizing dopant evaporation. After optimizing laser sintering process parameters, the best electrical conductivity, thermal conductivity, and Seebeck coefficient were found to be 70.42 S/cm, 0.84 W/m K, and 133.7  $\mu$ V/K, respectively. We demonstrate that laser sintered SiGe thin films have low thermal conductivity while maintaining good electrical conductivity for high temperature thermoelectric applications. Published by AIP Publishing. <https://doi.org/10.1063/1.5018337>

## I. INTRODUCTION

Silicon germanium (SiGe) plays an important role in high temperature thermoelectric devices. Current applications of SiGe include the Radioisotope Thermoelectric Generators (RTGs) being used by NASA to convert heat generated from the decay of radioactive isotopes into electricity on deep space missions.<sup>1</sup> Generating electricity from waste heat using thermoelectric devices is also an attractive alternative energy source. For example, thermoelectric materials could be used in automobiles to harvest waste heat to power electrical systems in the car, thus improving fuel economy and lowering of greenhouse gas emission.

One of the major problems with current thermoelectric systems is the low conversion efficiency. The efficiency of thermoelectric materials is quantified by a dimensionless figure of merit, ZT. In order to achieve high ZT, a material must have a high Seebeck coefficient, high electrical conductivity, and low thermal conductivity. In recent years, studies have shown that nanocrystalline materials can have better figure of merits than their bulk counterparts.<sup>2</sup> In nanocrystalline materials, phonon scattering is enhanced at grain interfaces, thus reducing the part of the thermal conductivity contributed by phonons  $\kappa_p$ .<sup>3</sup> The resulting effect being that the overall thermal conductivity may be reduced without significantly affecting the electrical conductivity.

Previous work by NASA found ZT = 0.7 at 650 °C (Ref. 4) in bulk SiGe with grain sizes on the order of 1–10  $\mu$ m; while an MIT research group, using a bulk material with a 20 nm grain size, found ZT = 0.75 at 650 °C for p-type

(maximum ZT = 0.95 at 900 °C),<sup>5</sup> and ZT = 1.05 at 650 °C for n-type (maximum ZT = 1.3 at 900 °C),<sup>6</sup> the highest recorded SiGe figure of merit. The Field Assisted Sintering Technique (FAST) was used to make bulk materials with nano-grain structures in both studies.

Lasers have been proved to be a successful tool for large scale manufacturing,<sup>7</sup> because of their low cost, high efficiency, high throughput, and easy operation. In renewable energy applications, laser processing was reported to perform laser doping,<sup>8</sup> laser transferring,<sup>9</sup> and laser texturing.<sup>10</sup> In this work, thin films made of plasma synthesized Si<sub>80</sub>Ge<sub>20</sub> nanoparticles doped with phosphorous were sintered by a long pulsed infrared laser. We demonstrate that laser sintered SiGe thin films have high electrical conductivity and low thermal conductivity. Also, the impact of surface morphology on electrical and thermal conductivity was investigated.

## II. EXPERIMENTAL

Hydrogen terminated Si<sub>80</sub>Ge<sub>20</sub> nanocrystals with 5% nominal phosphorous doping were grown in a capacitively coupled plasma tube reactor and deposited onto a quartz substrate in porous thin films, as described in previous literature.<sup>11</sup> The average crystallite size, surface morphology, elemental composition, and distribution were found with XRD, SEM, TEM, and FTIR, respectively.

To investigate the structure and the degree of alloying of raw films, SiGe nanocrystals (NCs) were deposited directly onto carbon-coated copper TEM grids (thin carbon/holey support) and transferred with less than 30 s of air exposure into an aberration-corrected FEI Titan G2 60-300 (scanning) transmission electron microscope (STEM) equipped with a Super-X

<sup>a)</sup>Electronic mail: mgupta@virginia.edu

energy-dispersive X-ray (EDX) detector. High-angle annular dark field (HAADF) STEM images were acquired at 200 kV (imaging only) and 60 kV (elemental mapping) with a 25 mrad convergence semi-angle and an 80 pA beam current. Spatially resolved STEM-EDX maps of individual particles were acquired with  $350 \times 350$  pixels over a  $15 \times 15 \text{ nm}^2$  area with a pixel dwell time of  $3 \mu\text{s}/\text{pixel}$ , acquisition time of 10 min, and drift correction after every frame. The K-edges of Si, Ge, and O were background-subtracted and integrated, producing elemental maps. A three-pixel Gaussian blur was applied to the images shown in Fig. 1 to aid in visualization. The data for each element were radially averaged around the center of the particle to obtain the radial map shown in Fig. 1(d).

An infrared long pulse laser of wavelength 1070 nm was chosen for this study because it can heat a large thickness of the film, which will provide better sintering uniformity. There are two major benefits to using a long pulse laser instead of a short pulse laser. First, the thermal effect of the long pulse laser lasts longer than the short pulse laser, resulting in a deeper penetration depth. Additionally, the longer thermal duration will provide better uniformity. Second, the thermal effect of the long pulse laser works better as an annealing method and will improve the film's crystal structure.

The films were sintered by a quasi-continuous wave (QCW) laser (IPG photonics YLR-150/1500-QCW-AC) with

a 1070 nm wavelength, a Gaussian profile, and a pulse duration of 0.1 ms. The peak power of the laser was 1500 W at a 100%~set point, and the pulse repetition rate (PRR) was between 100 Hz and 1000 Hz, depending on the experiment. For long pulse and CW lasers, both the peak power and the average power are important. The heating effect of the laser was varied by the laser peak power, PRR, pulse width, spot size, and sample scanning speed. The beam was first reflected by a mirror before passing through a lens with a focal point 3 cm above the sample. This focal point was chosen to decrease the laser intensity at the surface of the sample and increase the area covered by beam scanning. The sample chamber was mounted beneath the beam on a computer controlled x-y stage, allowing for smooth rastering of the sample. The sample was covered with a quartz slide to reduce dopant and film loss and the chamber was pumped down to  $10^{-2}$  Torr before being purged with argon gas. Low flow argon gas was then maintained throughout the sintering process to reduce oxidation of the sample. A schematic of this experimental setup is shown in Fig. 2.

The electrical conductivity of the film was measured using the 4-point probe method. An FEI Quanta 650 Scanning Electron Microscope (SEM) was used to characterize the surface morphology. The relationship between the surface morphology and the electrical conductivity is discussed in Sec. III.

The thermal conductivity of the thin films was determined using the 3 omega method,<sup>12</sup> as shown in Fig. 3. A 650 nm thick photoresist SU-8 was spin coated onto the film and thermally cured to serve as the insulation layer. Then, the silver heater pattern was transferred onto the sample device and the reference device by photolithography.<sup>13</sup> An alternating current with angular frequency  $\omega$  was applied to the silver heater. The temperature rise can be described by the following:

$$\Delta T = 2 \frac{dT}{dR} R \frac{V_{3\omega}}{V_{1\omega}}, \quad (1)$$

where  $R$  is the electrical resistance,  $RdT/dR$  is the reciprocal of the temperature coefficient of resistance (TCR) of the

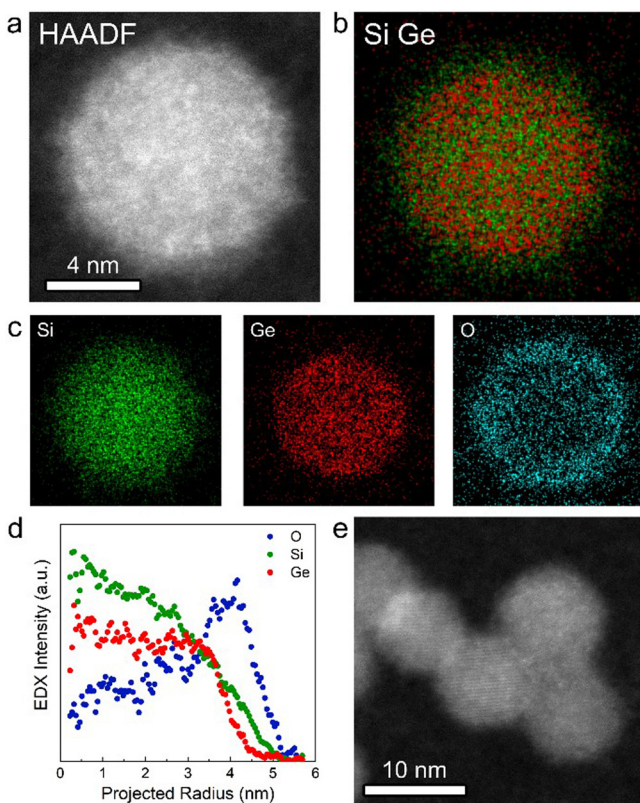


FIG. 1. Representative STEM-EDX analysis. (a) 60 kV HAADF image of a 5% (nominal) P-doped  $\text{Si}_{80}\text{Ge}_{20}$  NC, showing spherical geometry and no obvious elemental segregation. (b) Composite map of Si (green) and Ge (red). (c) Independent elemental maps of Si, Ge, and O. (d) Radially averaged EDX intensity, confirming a relatively uniform distribution of Si and Ge throughout the NC as well as the presence of a thin  $\sim 1$  nm oxide layer. (e) 200 kV HAADF-STEM image of a different cluster of 8–10 nm diameter spherical NCs, showing single crystal lattice fringes and uniform alloying.

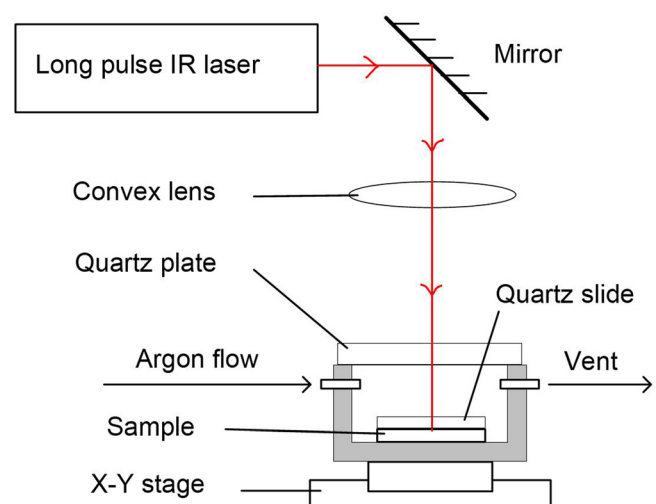


FIG. 2. Schematic of the experimental setup used to laser sinter SiGe films.



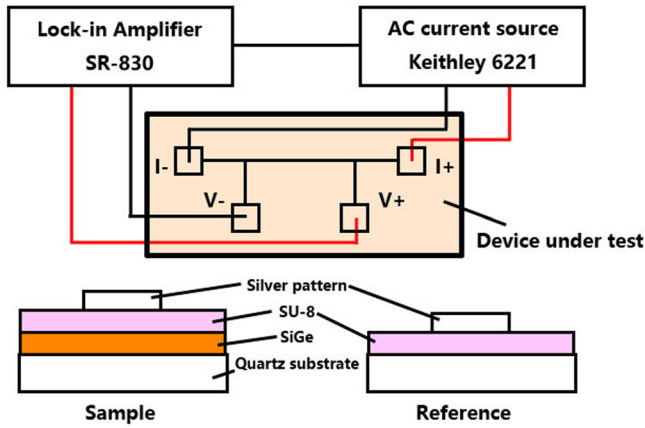


FIG. 3. Schematic of the differential 3 omega measurement setup.

silver heater, and  $V_{1\omega}$  and  $V_{3\omega}$  are the first and third harmonic voltage. The temperature rise through the SiGe film  $\Delta T_f$  can be derived as follows:<sup>13</sup>

$$\Delta T_f = \Delta T_{\text{sample}} - \frac{P_{\text{sample}}}{P_{\text{ref}}} \Delta T_{\text{ref}}, \quad (2)$$

where  $\Delta T_{\text{sample}}$  is the temperature rise in the sample device and  $\Delta T_{\text{ref}}$  is the temperature rise in the reference device. Therefore, temperature rise through the SiGe film  $\Delta T_f$  can be calculated by subtracting the  $\Delta T_{\text{ref}}$  from  $\Delta T_{\text{sample}}$ .  $P_{\text{sample}}$  and  $P_{\text{ref}}$  are the thermal powers applied to the sample device and to the reference device, respectively. In order to simplify the calculation and minimize the heat loss error, both thermal powers can be adjusted to the same value. Then, the thermal conductivity can be derived by the following:

$$\kappa = \frac{P_{\text{sample}} t_f}{Lw\Delta T}, \quad (3)$$

where  $t_f$  is the film thickness,  $L$  is the length of the heater, and  $w$  is the width of the heater.

The Seebeck coefficient measurement setup is shown in Fig. 4. One side of the sample was mounted on the heating element, and the other side was attached to a heat sink. Two probes were attached on the film. Different temperature gradients were generated and controlled by the thermal module.

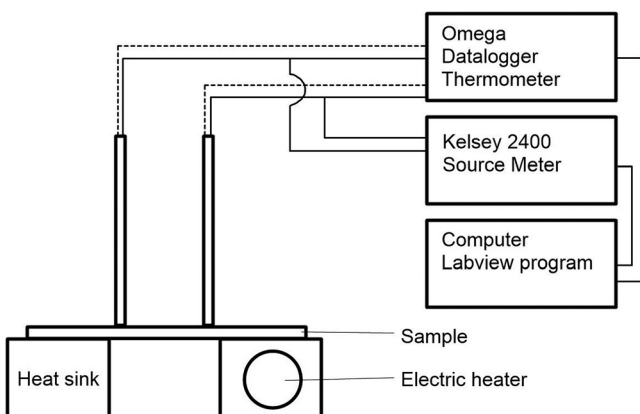


FIG. 4. Schematic of the Seebeck coefficient measurement setup.

The temperatures of hot/cold side and the thermal voltage are measured by an Omega datalogger thermometer, and a Kelsey 2400 Source meter, separately. The results are recorded using a LabVIEW program.

### III. RESULTS AND DISCUSSION

#### A. Plasma synthesized nanocrystalline SiGe thin film properties

The nanocrystals composing the film were found to be crystalline, spherical, and well alloyed and had an average crystallite size of 8 nm with a 10%–15% standard deviation as shown in Fig. 1. Past research on this synthesis method has found the active dopant levels in the synthesized nanoparticle films to be lower than the nominal levels with the phosphorous dopants included via lattice substitution.<sup>14</sup> Minor exposures to air between processing steps resulted in some surface oxidation of the nanocrystals, as shown in Fig. 1.<sup>14</sup>

Films were found to be between 3 and 10  $\mu\text{m}$  thick, depending on the deposition time, uniform on the scale required for sintering and extremely porous. These thicknesses are significantly larger than those of other published thin film type thermoelectric materials.<sup>15–19</sup> Thicker films may allow for a larger temperature gradient to be obtained thus increasing the thermovoltage output. The high porosity of the films combined with the deactivation of charge carriers during minor oxidation resulted in immeasurably low electrical conductivity of the pre-sintered films.<sup>14</sup>

#### B. Effects of sintering by a long pulse laser

The high energy imparted to the SiGe films by the long pulse laser during sintering resulted in the melting of the films. During the melting and the cooling process that followed the constituent elements of the films were reordered. The relatively lower melting temperature of the germanium caused it to transition from liquid to solid form before the silicon. This caused the germanium to segregate out of the SiGe alloy, forming balls of a germanium rich material in some cases and webbing patterns of a germanium rich material in other cases. This can be seen in the backscattering SEM images in Fig. 5 where the germanium rich materials appear whiter than the silicon rich. In addition to modifying

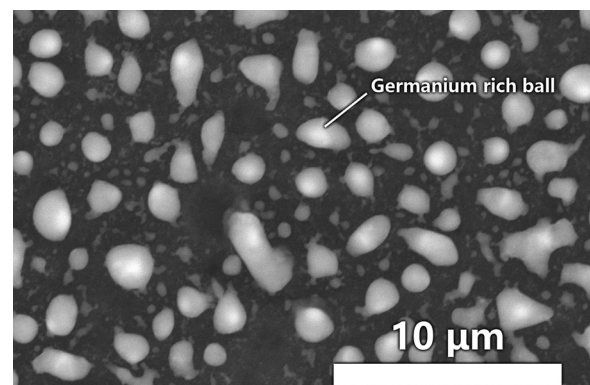


FIG. 5. SEM, in back scatter mode, images of the balling structure. The laser parameters were 225 W peak power, 300 Hz PRR, 0.1 ms pulse width, and 0.5 mm/s scanning speed.

the alloy fraction of the SiGe, the temperature needed to melt the material far surpasses the melting temperature of the phosphorous dopant. The high heat could cause one of two effects; some dopants could evaporate out of the material with further increase in absorbed laser energy imparted to the film causing high loss of dopants. Although the quantitative result of dopant loss was difficult to measure because of the high porosity, the dopant loss was qualitatively observed by performing Energy-dispersive X-ray spectroscopy (EDS) before and after the laser sintering process; alternatively, phosphorous atoms that were previously not four fold substitutionally incorporated into the crystal lattice could be better incorporated into the lattice structure after laser processing. This would result in an increase in electrical conductivity due to activated dopant atoms and improved conductive paths.

In order to understand the processes of dopant reactivation and dopant loss, several attempts were made to measure the dopant concentration of post sintered samples. However, the porosity and rough surface of the samples make it not ideal for secondary-ion mass spectrometry (SIMS). Meanwhile, the low concentration of phosphorus is too close to the confidence limits of Energy-dispersive X-ray spectroscopy (EDS) and X-ray photoelectron spectroscopy (XPS) to get an accurate quantitative measure.

### C. Segregation of germanium

A Gaussian beam shape is good for process parameter optimization in lab experiments because it can sinter the film with different laser energy densities in one scan. The process of the germanium segregation can be seen in Figs. 6(a) to 6(d). The figure shows the impact of the Gaussian beam profile and surface morphology variation. It also shows different surface morphologies after sintering with different laser energy densities. All figures were taken under SEM back scatter mode. The brighter parts have a higher average atomic number, and the darker parts have lower average atomic number. The thickness of the films is measured at 3–5  $\mu\text{m}$ , which is larger than the penetration depth of SEM predicted by the Kanaya-Okayama formula.<sup>20</sup> Therefore, brighter areas in the figure show germanium rich regions, while darker areas show silicon rich regions. Figure 6(d) shows the film sintered by the peak of Gaussian beam, where the laser energy density was the highest. The maximum sintering temperature of location (d) was higher than that of location (a), the edge of the Gaussian beam. When the temperature was relatively low, the germanium phase had a low viscosity and could only form small islands, as shown in Fig. 6(a). The electrical conductivity was close to that of the raw film because the islands were separated from each other and no conductive path was formed. When the temperature became higher, there were two possibilities. If the germanium rich phases wet the substrate well, a semi-continuous percolation structure is formed. This structure had high electrical conductivity. This could be because of better connected pathways and limited dopant evaporation. However, if the germanium rich phases did not wet the substrate well, the previously mentioned small islands of germanium began

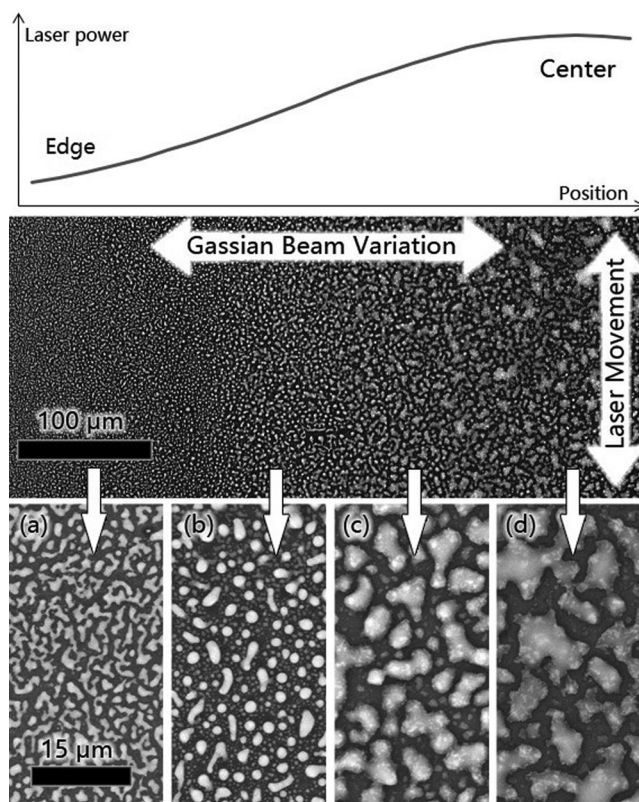


FIG. 6. SEM, in back scatter mode, images of the surface morphology changes due to the Gaussian beam profile. Brighter areas show germanium rich regions, while darker areas show silicon rich regions. (a) shows the films sintered by the edge of the Gaussian beam, with (b)–(c) approaching the center of the beam and (d) showing the film sintered by the center of the Gaussian beam. The incident Gaussian beam power profile is plotted at the top.

to merge together and formed small balls, as shown in Fig. 6(b). When the laser energy density was even higher, the small balls began to merge together and formed large islands, as shown in Figs. 6(c) and 6(d). Meanwhile, the high processing temperature would result in too much dopant loss. Lack of a conductive path and too low dopant concentration resulted in a near zero electrical conductivity.

### D. Surface morphology and electrical conductivity

Some sintering experiments resulted in the balling structure as seen in Fig. 4. This surface morphology shows segregation and discontinuity, resulting in an electrical conductivity too small to be measured. This could be due to a variety of factors. Poorly chosen sintering parameters or improper cleaning of the substrate surface could both cause balling. The quartz substrate was also a potential cause of this balling structure as the molten silicon germanium did not wet the quartz well.

The percolation structure shown in Fig. 7 is a more desirable structure. The results shown in Figs. 7(a) to 7(c) were sintered with the same laser peak power of 225 W, the same scanning speed of 0.5 mm/s, but different PRRs (a) 200 Hz, (b) 400 Hz, and (c) 800 Hz. The corresponding tilted-view SEM images are shown on the right. The SEM images were taken using the back scattering mode that allows for some elemental analysis. The bright parts contain more germanium,



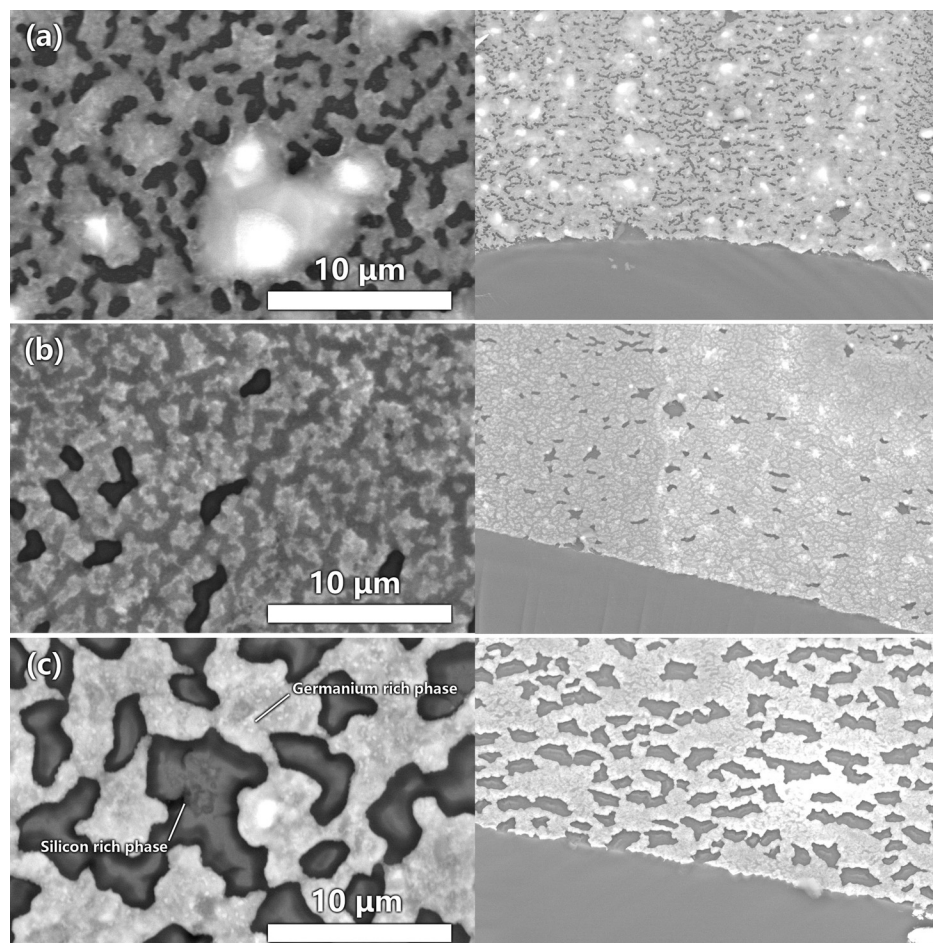


FIG. 7. SEM, in back scatter mode, image of SiGe nanoparticles, (a) before sintering, (b) before sintering at higher magnification, and (c) after laser sintering. The right figures are at lower magnification and tilted-view image.

while the dark parts contain more silicon. Figures 7(a) and 7(c) have much lower electrical conductivities when compared with Fig. 7(b) but the mechanisms are very different. Figure 7(a) shows the balling structure beginning to appear because of bad substrate wetting. In Fig. 7(c), the surface morphology shows that the laser intensity was too high, resulting in elemental segregation and accumulations of germanium. Although the conductive regions are still interconnected, there are fewer conductive paths and they are narrower than those in Fig. 7(b). Thus, the electrical conductivity of (c) was lower than that of (b). Figure 7(b) shows the best surface morphology as well as the best electrical conductivity because of selection of proper laser parameters. The nanoparticles were interconnected and the surface was more uniform. The process temperature was also high enough to reactivate dopant atoms. The best electrical conductivity found in this study was 70.42 S/cm.

#### E. Seebeck coefficient, thermal conductivity, and figure of merit ZT

The Seebeck coefficient was measured at room temperature. The temperature at the hot side of the sample was varied from 301 K to 310 K, and the cold side was held at 300 K, which gives a temperature difference from 1 K to 10 K. At least two heating-cooling cycles were performed to improve the measurement accuracy. The Seebeck coefficient of the post sintered films was 133.7  $\mu\text{V/K}$ , compared to

140  $\mu\text{V/K}$  before sintering. The Seebeck coefficient is primarily determined by the composition of the film.<sup>15</sup> The Seebeck coefficient in this study is on the same order of magnitude compared with other published works.<sup>4,6,13,15,21</sup>

The thermal conductivity was calculated using Eq. (3). The effective thermal conductivity of the champion thin film was calculated to be 0.84 W/m K, which is significantly lower than the previously reported 2.5 W/m K in 2008 (Ref. 16) and 4.5 W/m K in the bulk RTGs used by NASA.<sup>5</sup> The sub-micron range grain size obtained after laser sintering, as

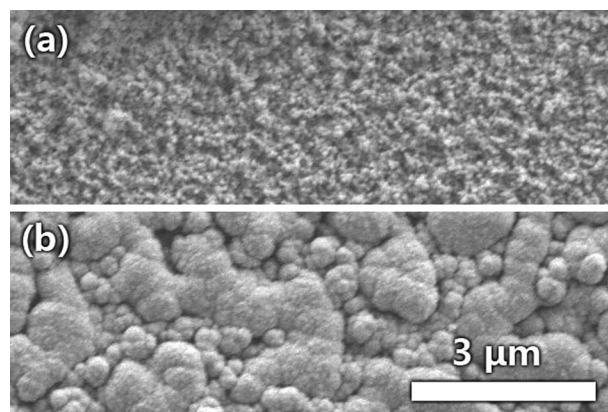


FIG. 8. SEM, in secondary electron mode, image of SiGe nanoparticles, (a) before sintering and (b) after laser sintering. The scale bar is applied to both figures.

TABLE I. Comparison of thermoelectric data for bulk and thin film SiGe.

References	Materials	Method	Doping	Type	Seebeck $\mu\text{V/K}$	$\sigma$ S/cm	$\kappa$ W/m K	TK	ZT	Note
This work	Si <sub>80</sub> Ge <sub>20</sub>	Laser sintering	n	Film	133.7	70.42	0.83	300	0.05	a
17	Si <sub>70</sub> Ge <sub>30</sub>	LPCVD	p	Film	131	346	4.7	300	0.04	a
17	Si <sub>70</sub> Ge <sub>30</sub>	LPCVD	n	Film	179	342	5.1	300	0.06	a
18	Si <sub>70</sub> Ge <sub>30</sub>	LPCVD	p	Film	35	909	3.5	300	0.01	a
18	Si <sub>70</sub> Ge <sub>30</sub>	LPCVD	n	Film	190	161	3.5	300	0.05	a
19	Si <sub>80</sub> Ge <sub>20</sub>	LPCVD	p	Film	220	30	2.9	300	0.02	a
15, 22, 23	Si <sub>78</sub> Ge <sub>22</sub>	Laser sintering	n	Film	160–180	15	0.05	300		b
6	RTG			Bulk	100–120	1200	4.5	300	0.09	ZT = 0.9 at 1200 K
6	Si <sub>80</sub> Ge <sub>20</sub>	FAST	n	Bulk	100–120	625–825	2.5	300	0.1	ZT = 1.3 at 1200 K
5	Si <sub>80</sub> Ge <sub>20</sub>	FAST	p	Bulk	110–130	800–900	2.25–2.6	300	0.15	ZT = 1 at 1100 K
24	SiGe	FAST	n	Bulk	80–130	900–1650	3.9–6.25	300	0.06	ZT = 1.3 at 1200 K
21	SiGe	FAST	n	Bulk	104	1140	3.94	300	0.09	a
4	Si <sub>80</sub> Ge <sub>20</sub>	FAST	n	Bulk	175	140	1.8	300	0.07	ZT = 0.8 at 1300 K

<sup>a</sup>No high temperature data.

<sup>b</sup>Not measured for the same sample.

shown in Fig. 8, and the high porosity of these films both contribute to the low thermal conductivity value.

For our champion device, the figure of merit ZT can be calculated from the electrical conductivity 70.42 S/cm, effective thermal conductivity 0.84 W/m K, and the Seebeck coefficient 133.7  $\mu\text{V/K}$ . With  $ZT = \frac{\alpha^2}{\kappa} T$ , the figure of merit of the champion thin film at room temperature is 0.05. This number is comparable to other published works,<sup>4,6,13,15,21</sup> which is from 0.01–0.06. This result suggests that laser sintering provides an easy and economical way to synthesize thermoelectric materials compared to more expensive and time-consuming methods like FAST and Low Pressure Chemical Vapor Deposition (LPCVD).

## F. Discussion

Table I compares the results of this work with the thermoelectric properties of bulk and thin films SiGe reported by other researchers. The electrical conductivity of SiGe thin films is about 1 order of magnitude smaller than that of bulk SiGe. An important factor that may impact the electrical conductivity is the porosity.<sup>21</sup> The Field assisted sintering technique (FAST) for bulk SiGe synthesis involves mechanical pressure. Therefore, the porosity of bulk SiGe is usually much smaller than for thin films. On the other hand, the effective thermal conductivity will benefit from high porosity. The laser sintering process results in more porous samples when compared with Low Pressure Chemical Vapor Deposition (LPCVD). Therefore, laser sintering results in the smallest thermal conductivity.

In this work, the best electrical conductivity achieved was 70.42 S/cm, the effective thermal conductivity was 0.84 W/m K, and the Seebeck coefficient was 133.7  $\mu\text{V/K}$ . The thermal conductivity is significantly lower than the reported data shown in Table I, excepting the sample with a film thickness in the nanometer range. The electrical conductivity could be improved by starting with a less porous and smoother film. However, a less porous and smoother film may also enhance the thermal conductivity, and thus lead to a lowering of figure of merit ZT. Therefore, it is important to

find a balance between thermal conductivity and electrical conductivity. The figure of merit of the laser sintered SiGe films in this study was better than that reported with the same Si<sub>80</sub>Ge<sub>20</sub> ratio, and is only slightly lower than that of higher germanium content films.<sup>17</sup> However, with the cost of germanium significantly higher than that of silicon, Si<sub>80</sub>Ge<sub>20</sub> would be more desirable in large scale manufacturing.

It is worth mentioning that the method reported in this paper is suitable for manufacturing applications, because of the following unique advantages: (1) The overall size of the sample in this method is not limited by the pressure chamber as used in FAST; (2) The laser sintering is performed in atmospheric pressure with no vacuum requirement; (3) No wet chemical process is required; (4) The overall throughput is much higher than FAST; (5) Both raw film preparation and laser sintering can be adapted to be “printing” processes, which are suitable for automated production.

## IV. CONCLUSION

We have demonstrated that the laser sintering is a versatile method in fabricating SiGe thin films for thermoelectric applications. The laser peak energy, scanning speed, and PRR were optimized to maximize electrical conductivity and minimize thermal conductivity. In this study, the best electrical conductivity achieved was 70.42 S/cm, the lowest thermal conductivity was 0.84 W/m K, and the Seebeck coefficient was 133.7  $\mu\text{V/K}$ . The electrical conductivity was highly dependent on two major factors. The first factor was surface morphology. Interconnected percolation structures provided better conductive pathways, while balling structures resulted in electrical isolation. The second factor was dopant reactivation. Dopant atoms can get reactivated during laser sintering, but the evaporation under high temperature needs to be minimized. Thermal conductivity was found to be dramatically reduced by sub-micron grain sizes and high porosity. The overall process provides a fast, low cost, and easy way for SiGe thermoelectric thin film fabrication. The electrical conductivity of laser sintered SiGe films can be further improved by decreasing the porosity and increasing

the dopant concentration, which in turn could further improve the figure of merit.

## ACKNOWLEDGMENTS

We acknowledge R. Skinner (University of Minnesota) for synthesizing the raw films. We acknowledge the support of NSF under the Award No. ECCS-1408443. JTH was supported by the MRSEC program of the National Science Foundation under Award DMR-1420013. STEM analysis was performed in the College of Science and Engineering Characterization Facility of the University of Minnesota, which receives partial support from the NSF through the MRSEC program.

<sup>1</sup>C. Wood, *Rep. Prog. Phys.* **51**, 459 (1988).

<sup>2</sup>G. A. Slack and M. A. Hussain, *J. Appl. Phys.* **70**, 2694 (1991).

<sup>3</sup>G. Pernot, M. Stoffel, I. Savic, F. Pezzoli, P. Chen, G. Savelli, A. Jacquot, J. Schumann, U. Denker, and I. Mönch, *Nat. Mater.* **9**, 491 (2010).

<sup>4</sup>N. Stein, N. Petermann, R. Theissmann, G. Schierning, R. Schmechel, and H. Wiggers, *J. Mater. Res.* **26**, 1872 (2011).

<sup>5</sup>G. Joshi, H. Lee, Y. Lan, X. Wang, G. Zhu, D. Wang, R. W. Gould, D. C. Cuff, M. Y. Tang, M. S. Dresselhaus, G. Chen, and Z. Ren, *Nano Lett.* **8**, 4670 (2008).

<sup>6</sup>X. W. Wang, H. Lee, Y. C. Lan, G. H. Zhu, G. Joshi, D. Z. Wang, J. Yang, A. J. Muto, M. Y. Tang, J. Klatsky, S. Song, M. S. Dresselhaus, G. Chen, and Z. F. Ren, *Appl. Phys. Lett.* **93**, 193121 (2008).

<sup>7</sup>M. C. Gupta and D. E. Carlson, *MRS Energy & Sustainability* **2**, 2 (2015).

<sup>8</sup>K. Sun, Y. Bao, and M. C. Gupta, *Laser Doping of Germanium for Photodetector Applications* (International Society for Optics and Photonics, 2014), p. 918008.

<sup>9</sup>L. Wang, D. E. Carlson, and M. C. Gupta, *Prog. Photovoltaics* **23**, 61 (2015).

<sup>10</sup>P. O. Caffrey and M. C. Gupta, *Appl. Surf. Sci.* **314**, 40 (2014).

<sup>11</sup>D. J. Rowe and U. R. Kortshagen, *APL Mater.* **2**, 022104 (2014).

<sup>12</sup>D. G. Cahill, *Rev. Sci. Instrum.* **61**, 802 (1990).

<sup>13</sup>A. J. Zhou, W. H. Wang, B. Yang, J. Z. Li, and Q. Zhao, *Appl. Therm. Eng.* **98**, 683 (2016).

<sup>14</sup>N. J. Kramer, K. S. Schramke, and U. R. Kortshagen, *Nano Lett.* **15**, 5597 (2015).

<sup>15</sup>B. Stoib, T. Langmann, S. Matich, T. Antesberger, N. Stein, S. Angst, N. Petermann, R. Schmechel, G. Schierning, D. E. Wolf, H. Wiggers, M. Stutzmann, and M. S. Brandt, *Appl. Phys. Lett.* **100**, 231907 (2012).

<sup>16</sup>R. Cheaito, J. C. Duda, T. E. Beechem, K. Hattar, J. F. Ihlefeld, D. L. Medlin, M. A. Rodriguez, M. J. Champion, E. S. Piekos, and P. E. Hopkins, *Phys. Rev. Lett.* **109**, 195901 (2012).

<sup>17</sup>J. Xie, C. Lee, M. F. Wang, Y. H. Liu, and H. H. Feng, *J. Micromech. Microeng.* **19**, 125029 (2009).

<sup>18</sup>Z. Y. Wang, P. Fiorini, V. Leonov, and C. Van Hoof, *J. Micromech. Microeng.* **19**, 094011 (2009).

<sup>19</sup>M. Takashiri, T. Borca-Tasciuc, A. Jacquot, K. Miyazaki, and G. Chen, *J. Appl. Phys.* **100**, 054315 (2006).

<sup>20</sup>K. Kanaya and S. Okayama, *J. Phys. D: Appl. Phys.* **5**, 43 (1972).

<sup>21</sup>H. Lee, D. Wang, W. Wang, Z. Ren, B. Klotz, M. Y. Tang, R. Yang, P. Gogna, J.-P. Fleurial, and M. S. Dresselhaus, *Thermoelectric Properties of Si/Ge Nano-Composite* (IEEE, 2005), p. 269.

<sup>22</sup>G. Schierning, J. Stoetzel, R. Chavez, V. Kessler, J. Hall, R. Schmechel, T. Schneider, N. Petermann, H. Wiggers, S. Angst, D. E. Wolf, B. Stoib, A. Greppmair, M. Stutzmann, and M. S. Brandt, *Phys. Status Solidi A* **213**, 497 (2016).

<sup>23</sup>B. Stoib, S. Filser, N. Petermann, H. Wiggers, M. Stutzmann, and M. S. Brandt, *Appl. Phys. Lett.* **104**, 161907 (2014).

<sup>24</sup>B. Yu, M. Zebarjadi, H. Wang, K. Lukas, H. Wang, D. Wang, C. Opeil, M. Dresselhaus, G. Chen, and Z. Ren, *Nano Lett.* **12**, 2077 (2012).